Eur. Phys. J. D **6**, 63–76 (1999)

THE EUROPEAN PHYSICAL JOURNAL D

EDP Sciences

Frequency measurements of hyperfine splittings in ground rovibronic states of I_2 by stimulated resonant Raman spectroscopy

J.-P. Wallerand[1], F. du Burck[1,a], B. Mercier[1], A.N. Goncharov[1,2], M. Himbert[1], and Ch.J. Bordé[1,b]

[1] Laboratoire de Physique des Lasers, Université Paris-Nord, Avenue J.-B. Clément, 93430 Villetaneuse, France
[2] Institute of Laser Physics, Siberian Branch of the Russian Academy of Sciences, Novosibirsk, Russia

Received: 26 September 1998 / Received in final form: 30 November 1998

Abstract. Measurements of hyperfine splittings in the ground electronic state of I_2 have been performed by stimulated Raman spectroscopy. An argon laser emitting at 514.5 nm, drives the coherence between hyperfine levels of the $J'' = 13$ or $J'' = 15$ rotational levels of the ground vibronic state, *via* resonant excitation of the hyperfine transitions of the optical resonances (43-0) P(13) or R(15). We study the influence of the various experimental parameters on the line shape: the beam geometry, the laser modulation spectrum, the laser power, the molecular frequency shifts. We show that only beam aberrations can give rise to a significant asymmetry of the line shape, which contributes to an error in the determination of the resonance frequency. From a theoretical expression of the line shape taking into account the beam geometry, a detailed study of this error is performed. The theoretical predictions and the experimental results are in very good agreement. From the measurements, improved sets of hyperfine interaction constants for the I_2 molecule have been calculated for $J'' = 13$ and $J'' = 15$. These constants are identical for both levels, except for quadrupole coupling constant eqQ which exhibits a J-dependence, which we attribute to the centrifugal distortion of the molecule.

PACS. 33.15.Pw Fine and hyperfine structure – 33.70.Jg Line and band widths, shapes, and shifts

1 Introduction

This paper, which is a sequel to reference [1], offers an improved and enlarged set of accurate measurements of hyperfine splittings in the ground electronic state of I_2 obtained by stimulated Raman spectroscopy.

A stimulated Raman resonance is induced in the three-level molecular system of Figure 1 by two copropagating laser beams at angular frequencies ω_1 and ω_2, tuned respectively to the optical transitions a-b and a'-b. In our case, the levels a and a' are hyperfine sublevels of ground rovibronic states of I_2 ($X\ ^1\Sigma_{0^+g}$, $v'' = 0$, $J'' = 13$ or $J'' = 15$) and the level b, which is common to both transitions, belongs to the excited electronic state ($B\ ^3\Pi_{0^+u}$, $v' = 43$, $J' = 12$ or $J' = 16$). The optical transitions a-b and a'-b are thus hyperfine components of the P(13) and R(15) lines of iodine near 514.5 nm (Fig. 2) easily excited by an argon laser. Beam 1 (ω_1) is resonant with the strong transition ($\Delta F = \Delta J = \pm 1$, $\Delta\varepsilon = 0$) while beam 2 (ω_2) is resonant with the weak transition ($\Delta F = 0$, $\Delta\varepsilon = 0$). The measured hyperfine splittings of the ground state $\omega_{a'a}/2\pi$ range between 27 and 458 MHz.

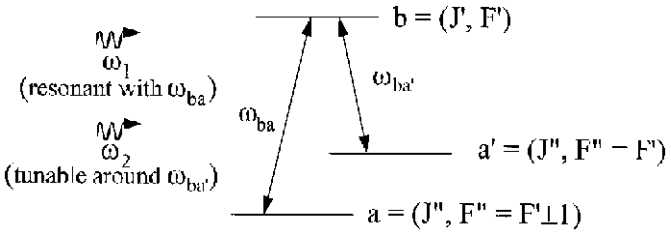

Fig. 1. Schematic representation of the stimulated resonant Raman interaction process involving hyperfine levels.

A theoretical line shape has been established in our previous studies for Raman spectroscopy with Gaussian laser beams. It has enabled us to understand and study all the effects resulting from the molecular motion, especially the influence of the wave front curvature, and to compare precisely calculated and experimental line shapes. We have found that the control of the laser beam geometry is crucial for the resolution and for the accuracy of the measurements. This careful study of the influence of the experimental parameters, together with an important improvement of optical adjustment and control, has resulted in a standard uncertainty close to 30 Hz for the Raman frequencies.

[a] e-mail: duburck@lpl.univ-paris13.fr
[b] e-mail: chbo@ccr.jussieu.fr

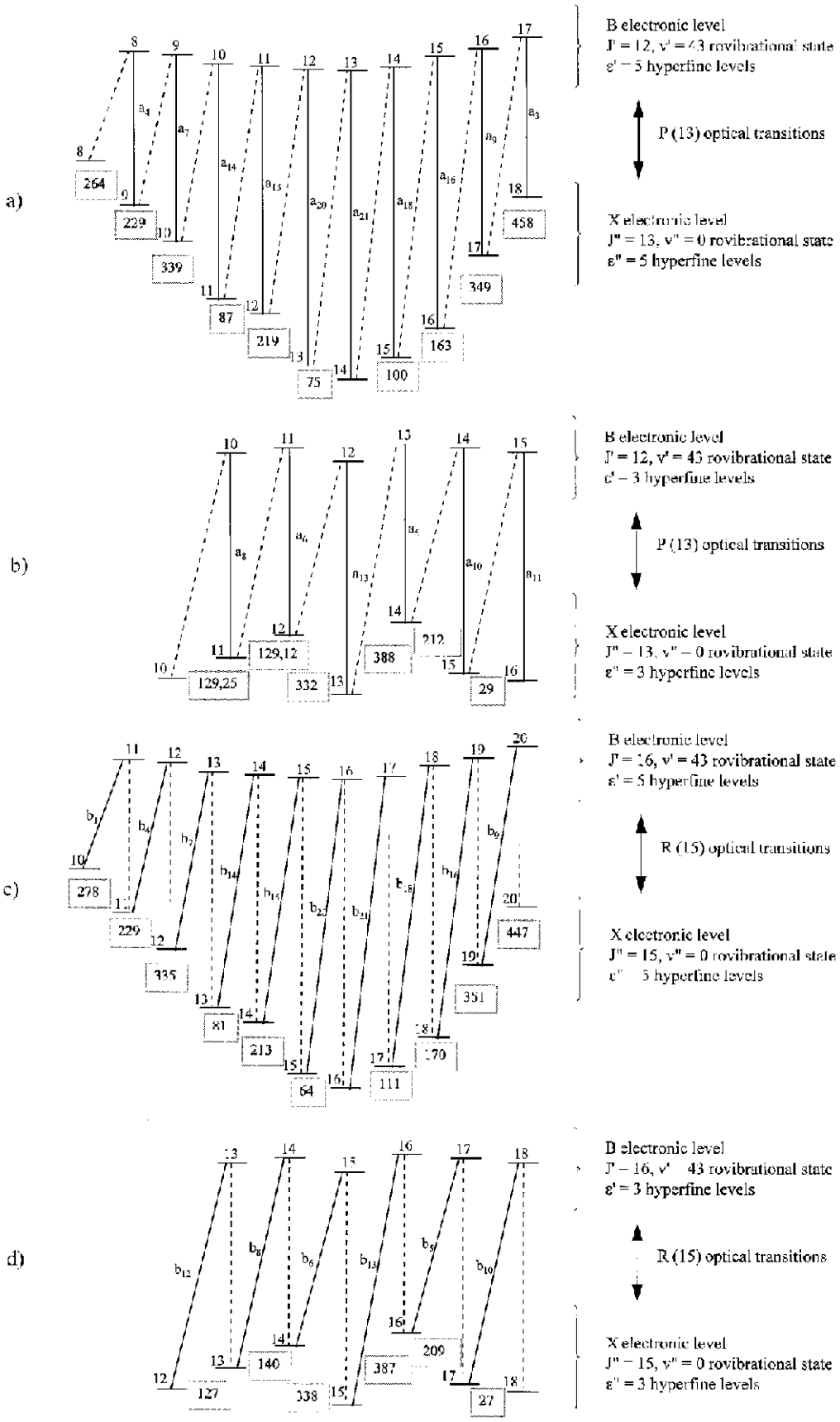

Fig. 2. Hyperfine levels implied in the Raman resonances that we have studied, for different values of J and ε. All frequency differences that we have measured are displayed and expressed in MHz. The levels are labeled by their F quantum number. Solid lines correspond to strong transitions and broken ones to weak transitions.

$$I^{(\mathrm{mod})}(\Delta) = \sum_{p_1}\sum_{q_1}\sum_{p_2}\sum_{q_2} J_{p_1}(\beta_1)J_{q_1}(\beta_1)J_{p_2}(\beta_2)J_{q_2}(\beta_2)\mathrm{Re}e^{i[(p_1-q_1)\omega_{m1}-(p_2-q_2)\omega_{m2}]t} \times \int_0^{+\infty} d\tau \int_0^{+\infty} d\tau' \frac{e^{\{i(\Delta+(2q_1-p_1)\omega_{m1}-q_2\omega_{m2})-2\gamma_{ba}\}\tau} \times e^{\{i(\Delta+q_1\omega_{m1}-q_2\omega_{m2})-\gamma_{a'a}\}\tau'}}{1+\frac{u^2}{w^2(z)}(\tau'^2+2\tau\tau'+2\tau^2)-i\frac{ku^2}{R(z)}\tau(\tau+\tau')}, \quad (1)$$

Finally, we have used these measurements to determine hyperfine interaction constants for the rotational levels $J'' = 13$ and $J'' = 15$ of the ground vibronic state of I_2. This new set of constants is more accurate than all former determinations, including that of Yokozeki and Muenter [2]. We demonstrate, for the first time through a direct and accurate measurement, that two rovibronic levels of I_2 have different values for their electric quadrupolar constant eqQ, while their magnetic interaction constants are almost identical.

2 The Raman spectrometer

The experimental arrangement, displayed in Figure 3, has been designed to provide an excellent quality for the geometry of the laser beams and for the purity of I_2. Special care has been taken to improve the symmetry between the beams and ensure their wave front matching, with respect to our previous set-up [1].

The laser beams with angular frequencies ω_1 and ω_2 (beam 1 and beam 2) are generated from the same Ar^+ laser emitting at 514.5 nm, split along two arms, each of them containing an acousto-optic modulator (AOM). The influence of the frequency jitter of the laser is therefore eliminated. The laser frequency is prestabilized to that of a Fabry-Perot resonator mode, locked in turn to a saturated absorption line corresponding to a hyperfine transition of the P(13) or R(15) line of molecular iodine [3]. The choice of the locking frequency and of the AOMs carrier frequency is made to ensure the resonance with optical transitions. The frequency difference between the two beams assumed to be equal to the frequency separation between two hyperfine levels of the ground state, is in the range between 27 MHz and 458 MHz depending on the studied line. The AOMs are driven by frequency synthesizers, locked to a GPS reference.

The lengths of the two arms between the beam splitters are equal in order to ensure the same geometrical characteristics of the beams. A common 12.5 mm waist radius is obtained close to the center of the cell by means of a 50 mm objective (L_2) and of a 300 mm doublet (L_3). A 10 μm diameter pinhole is placed at the intermediate beam waist location between L_2 and L_3, in order to improve the wave fronts quality and the reproducibility of the adjustment of the beam geometry. The AOMs are located at the beam waists created by the lens L_1 to keep the alignment of the beams in the cell during the frequency scanning: the beams after the lens L_2 converge to one point, the image of the waists inside the AOMs, whatever the AOM deviation angle is. In the I_2 cell, the only effect of the scanning is a very small transversal shift which does not affect the parallelism of the beams.

The interaction zone of the laser beams with the iodine molecules is a 57 cm long and 5 cm diameter cell, with $\lambda/10$ flatness silica windows glued on the Pyrex tube. The iodine pressure is controlled by thermostabilization of a cold finger and in order to limit the presence of impurities, the cell is continuously pumped during the measurements. The pressure in the cell is about 0.13 Pa (1 mTorr).

To limit the detection noise, a frequency modulation at $\omega_{m1}/2\pi = 5$ kHz with a modulation index $\beta_1 \simeq 1$ is applied to beam 1 and the signal is detected on beam 2, which is swept around the frequency $\omega_{a'b}/2\pi$ over 40 kHz. Moreover, the influence of the amplitude noise of the laser is reduced by a balanced detection. The signal is then demodulated at the modulation frequency with a time constant usually equal to 0.3 s and is stored as a 100 points record. The experimental line shape used for the measurements is the average of ~ 10 frequency scans in both directions to cancel errors arising from hysteresis. The center of the fitted resonance provides the frequency difference $\omega_1 - \omega_2$ corresponding to the Raman frequency. Each result has been confirmed by a second measurement performed a few days later and always showed good agreement.

3 Line shape of stimulated Raman resonances

A general expression of the Raman line shape is derived in [1]. This expression was obtained from a third-order development of the density matrix equations, using a diagrammatic representation [4]. The line shape takes into account the geometrical parameters of the Gaussian beams and hence allows for the broadening and shift associated with the finite transit time and the wave front curvature. To incorporate the full physics relevant to our present experiments in a single formula, the line shape is rederived in appendix A in the case of frequency-modulated beams.

For matched beams ($w_1(z) = w_2(z) = w(z)$; $R_1(z) = R_2(z) = R(z)$), the line shape is given by formula (14) of appendix A:

see equation (1) above

where the detuning comes through the expression $\Delta = \frac{\omega_{ba}}{\omega_1}(\omega_1 - \omega_2) - \omega_{a'a}$, and where γ_{ba} and $\gamma_{a'a}$ are the decay rates of the coherences. The frequency modulations appear through their angular frequencies ω_{mj} and their

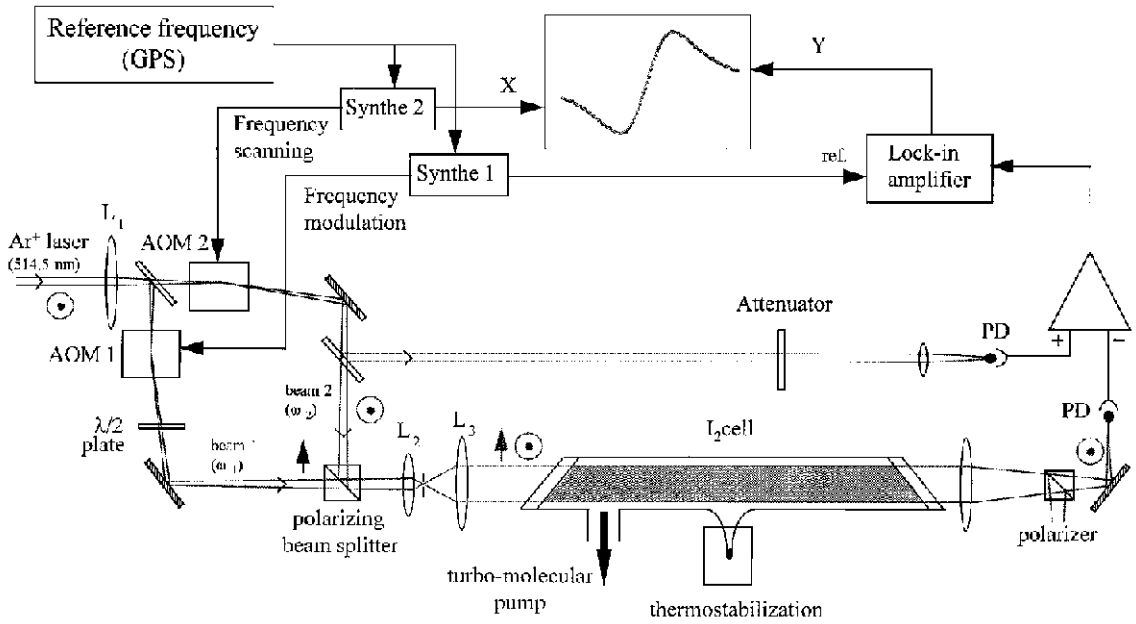

Fig. 3. Experimental set-up (AOM: acousto-optic modulator, PD: photodetector, synthe.: RF synthesizer, L_1: lens $f = 500$ mm, L_2: objective $f = 50$ mm, L_3: objective $f = 300$ mm).

modulation indices β_j. The line shape can also be written as a single integral (see formula (13) of appendix A).

The velocity u is the most probable velocity of the Maxwell-Boltzmann distribution in the cell ($u \simeq 140\,\mathrm{ms}^{-1}$ at 300 K for iodine) and k is the wave vector modulus.

In the real part of the denominator, the finite beam radius w leads to a transit time broadening of the line. In the imaginary part, the finite radius of curvature R of the wave front gives rise to a line shape distortion and to a resonance frequency shift. The various factors in the numerator describe the general frequency modulation case in which both beams are modulated. For the experiments that we have performed, only beam 1 was modulated, so that $\omega_{m2} = 0$ and $\beta_2 = 0$; $\omega_{m1} = \omega_m$ and $\beta_1 = \beta$. A detailed quantitative discussion of the signal size in this case will be given in another publication [5]. Here we will consider only the demodulated line shape for the first harmonic of the modulation frequency.

In the configuration of our measurements, the waist located in the I_2 cell has a radius w_0 equal to 12.5 mm (wave front curvature $\simeq 0$ and $\tau_{tr} \simeq 90$ μs) and the pressure in the cell is in the order of 0.13 Pa (1 mTorr) ($\gamma_{a'a}/2\pi \simeq 6$ kHz and $1/\gamma_{a'a} \simeq 25$ μs). These parameters result in an intermediate regime between collisional and transit-time limited regimes.

For the frequency measurement of hyperfine splittings, the modulation frequency was $\omega_m/2\pi = 5$ kHz. When ω_m and $\gamma_{a'a} \ll \gamma_{ba}$, and for a detection at the modulation frequency, the demodulated signal becomes

$$I^{(\mathrm{dem})}(\Delta) = \frac{1}{4\gamma_{ba}} \sum_q J_q(\beta) \times [\mathrm{Re}\{T(\Delta + q\omega_m)\}(J_{q-1}(\beta) + J_{q+1}(\beta)) \cos\varphi - \mathrm{Im}\{T(\Delta + q\omega_m)\}(J_{q-1}(\beta) - J_{q+1}(\beta)) \sin\varphi], \quad (2)$$

where φ is the detection phase and where

$$T(\Delta) = \frac{i\tau_{tr}}{2} \left\{ e^{(i\gamma_{a'a}+\Delta)\tau_{tr}} E_1[(i\gamma_{a'a} + \Delta)\tau_{tr}] - e^{-(i\gamma_{a'a}+\Delta)\tau_{tr}} E_1[-(i\gamma_{a'a} + \Delta)\tau_{tr}] \right\} \quad (3)$$

is the line shape in the absence of wave front curvature (see appendix A).

Figure 4 shows a typical experimental line shape corresponding to the transition (ε''=5, F''=9) $\leftrightarrow$ (ε''=5, F''=10) obtained with a modulation frequency $\omega_m/2\pi =$ 5 kHz and a modulation index $\beta = 1$. The iodine pressure in the cell was chosen to obtain a 7 kHz width (HWHM). The phase was adjusted to maximize the signal. The solid line in Figure 4(a) is a fit of the experimental data using (2) while the solid line in Figure 4(b) is a fit with a Lorentzian derivative. Although the line shape is not exactly the derivative of a Lorentzian, the two fits give the same central frequency. Thus, for simplicity, the practical determination of the values of the resonance frequencies has been performed with Lorentzian derivative fits.

4 Influence of the various experimental parameters on the accuracy of the frequency measurements

Various frequency shifts and distortions of the lines are of course responsible for errors in the center frequency measurement of the Raman resonances. We will see that the main effect is due to the beam wave front curvature and is well described by equation (1). In addition, we examine also how some other relevant phenomena such as the laser modulation spectrum, the laser power, the collisions, the

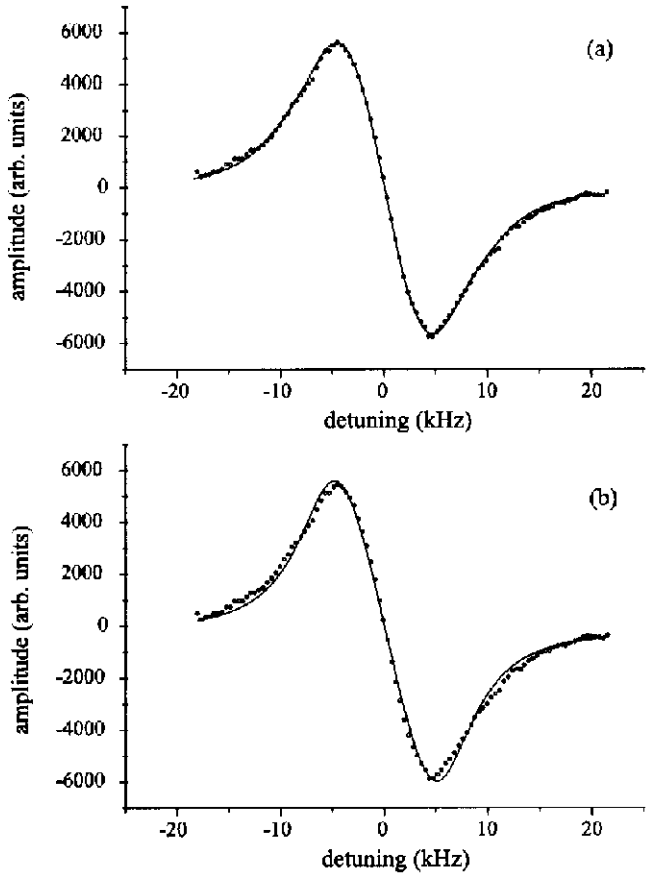

Fig. 4. Typical experimental Raman resonance corresponding to the transition $(\varepsilon'' = 5, F'' = 9) \leftrightarrow (\varepsilon'' = 5, F'' = 10)$ (circles) (modulation frequency: $f_m = 5$ kHz, modulation index: $\beta = 1$, lock-in amplifier time constant: 0.3 s). In (a), the calculated line shape (solid line) takes into account the frequency modulation applied to one of the beams; curve (b) is a fit with a 7 kHz wide Lorentzian derivative.

earth magnetic field perturb the line shape and what is their incidence on the determination of the line center.

4.1 Effects associated with the laser beam geometry

Any departure from the perfect geometry of colinear plane waves for the laser beams has the consequence that molecules see additional amplitude and phase modulations which may be classified into three categories.

4.1.1 Influence of an angle between the beams

As pointed out earlier, our experimental set-up is designed to ensure a good matching of the two beams at frequencies ω_1 and ω_2, thanks to the symmetry of their optical paths. The equality of the lengths of both arms and the fine tuning of the waist positions are obtained by focusing each beam through the 10 μm pinhole at the focus of the 300 mm objective. Besides wave front matching, this ensures the proper alignment of the beams and constrains their angle to be less than 3×10^{-6} rad.

An angle between the beams leads to a Doppler broadening of the lines. The line shape for plane waves is derived in [1] and, when $\gamma_{a'a} \ll \gamma_{ba}$ given by

$$I(\Delta) = \frac{1}{2\gamma_{ba}} \frac{\sqrt{\pi}}{ku\theta} \mathrm{Re}\left[W\left(\frac{\Delta + i\gamma_{a'a}}{ku\theta}\right)\right], \qquad (4)$$

where θ is the angle between the beams, k the wave vector modulus, u the most probable velocity and $W(z) = \exp\left[-z^2\right] \mathrm{erfc}\left[-iz\right]$ the error function of complex argument.

This line shape is a Voigt profile, evolving from a Lorentzian of HWHM equal to $\gamma_{a'a}/2\pi$ when $\gamma_{a'a} \gg ku\theta$ to a Gaussian curve of HWHM equal to $ku\theta\sqrt{ln2}/2\pi$ when $\gamma_{a'a} \ll ku\theta$.

The above upper limit of $3\cdot10^{-6}$ rad for the angle corresponds at most to a few hundred Hz broadening, which is presently negligible. In a cell, no line shift is associated to this broadening.

4.1.2 Transit time broadening

The line is also broadened by the finite time of interaction between the molecules and the laser beams. In the configuration of our measurements, the 12.5 mm waist radius results in a 1 kHz broadening to be compared with a collisional line width $\gamma_{a'a}/2\pi = 6$ kHz (HWHM).

4.1.3 Influence of the wave front curvature and of other aberrations

The divergence of the beams gives rise to an asymmetry of the line shapes which contributes to an error in the determination of the resonance frequency. Figure 5 displays the signal obtained with a 50 m radius of curvature of the wave front. The solid line in 5(a) is the result of a Lorentzian first derivative fit, which we currently use for the line center determination. One can see clearly the asymmetry of the experimental curve; as a consequence, the center of the Lorentzian fit is shifted by 500 Hz. By using formula (14), the lineshape distortion can be taken into account as illustrated by the solid line of Figure 5(b).

The beams divergence is determined by the position of the lens L_3 (Fig. 3). In order to adjust this divergence, we have used lateral shearing interferometry in which an interference pattern is obtained by superposing the two wave fronts sheared by a parallel glass plate [6]. By changing the distance between L_3 and L_2, one can obtain a fringeless pattern which guarantees a maximum radius of curvature. A pseudo line center is estimated by a fit with a Lorentzian derivative as was explained before. Figure 6 shows the difference between the true line center and this pseudo line center for an actual measurement versus $1/R$. On the same figure, we have plotted (solid line) the result of the same procedure of line center determination applied to the calculated line shape (14). The experimental and theoretical

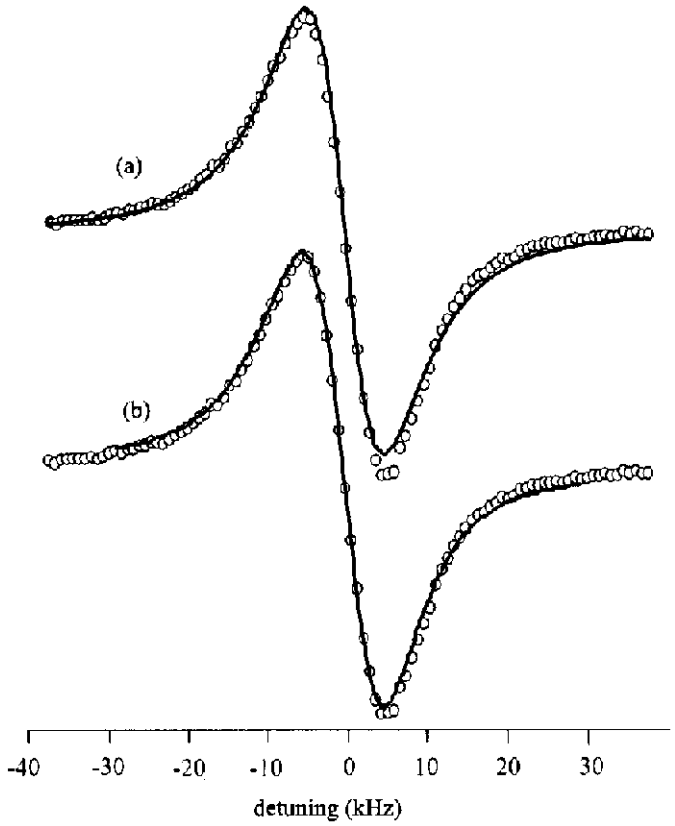

Fig. 5. Experimental Raman resonance ($\varepsilon'' = 5, F'' = 9$) $\leftrightarrow$ ($\varepsilon'' = 5, F'' = 10$) obtained with a 50 m radius of curvature of the wave front in the cell ($w_0 = 0.6$ mm at 50 m of the cell) (circles). (a): The solid line is the result of a fit with a Lorentzian derivative. The line center is shifted by 500 Hz. (b): The solid line is the result of the calculation with a Gaussian laser beam (see text).

curves are in very good agreement. From these curves we can estimate the uncertainty on the line center determination due to the uncertainty on the setting of the right distance between L_2 and L_3. This distance is adjusted with a standard deviation of 70 μm, which corresponds to $R = 1300$ m and to a frequency shift of 15 Hz.

The shearing interferometry provides a control of the maximum radius of curvature in all directions perpendicular to the propagation axis in order to suppress the astigmatism thanks to an angular adjustment of L_3. The only remaining aberration is then the spherical aberration of the L_3 objective. The maximum balanced aberration evaluated from the interference pattern is about $\lambda/4$. This deviation may be approximated by a fourth degree polynomial, with positive and negative local radii of curvature which compensate approximately. Using the relationship $\delta f_{(\mathrm{Hz})} = 20000/R_{(\mathrm{m})}$ representing the curve of Figure 6, we find an overall shift of 20 Hz, value that we retain as the uncertainty due to the geometrical aberrations.

In order to illustrate the importance of the beam geometry, we compare thirteen results of measurements with and without pinhole for the ($\varepsilon'' = 5$, $F'' = 9$) $\leftrightarrow$ ($\varepsilon'' = 5, F'' = 10$) splitting. In the first case, the standard deviation is only 15 Hz and in the second one 57 Hz (Fig. 7(a) and 7(b)). The pinhole fixes the geometry, improves the adjustments and minimizes the aberrations.

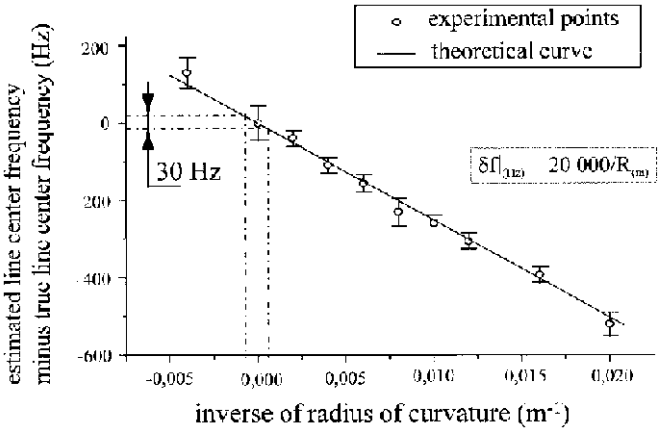

Fig. 6. Dependence of the line center frequency with the wave front radius of curvature (divergence). The circles are experimental measurements and the solid line is the theoretical shift. This shift is proportional to the curvature in the studied range $\Delta f_{(\mathrm{Hz})} = 20\ 000/R_{(\mathrm{m})}$.

4.2 Effects associated with the laser modulation spectrum

We have experimentally verified that a residual amplitude modulation of the laser beam has no appreciable effect on our measurements: first, a direct observation of the amplitude of the frequency-modulated beam (beam 1) has shown that this residual amplitude modulation percentage is much less than 1%; second, we have added purposely a 2% amplitude modulation to this beam and no measurable shift of the line center was detected.

4.3 Effects associated with the laser power

In order to study the effect of the laser power on the Raman line shape, higher-order terms have to be taken into account in the perturbative calculation of the line shape presented in appendix A. These terms are obtained from the diagrammatic representation by dressing either state a or a' with two or more interactions [7]. An example is shown in Figure 8 for a sixth-order calculation. The resulting effect is different depending whether these interactions are resonant or not with the transitions $a \leftrightarrow b$ and $a' \leftrightarrow b$. If $\beta = b$ (resonant case) in Figure 8, a broadening and an apparent splitting of the line appear as the laser power is increased. We found that the importance of this effect depends on which beam the detection is operated. If $\beta = b'$ (off-resonant case), a light shift of the line center manifests itself owing to the off-resonant coupling with the perturbing level b'.

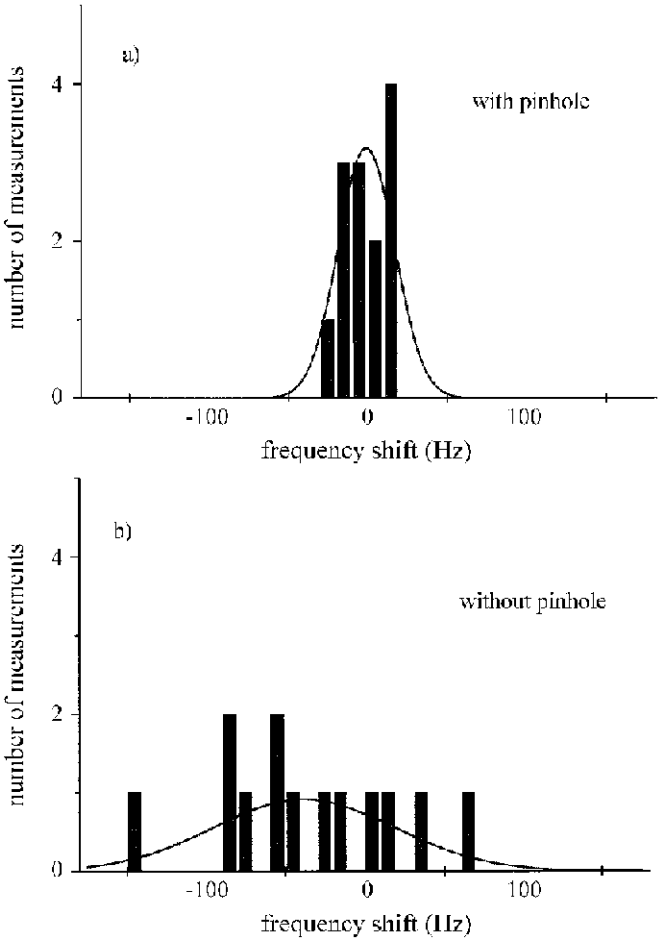

Fig. 7. Dispersion of the results with (a) and without (b) pinhole.

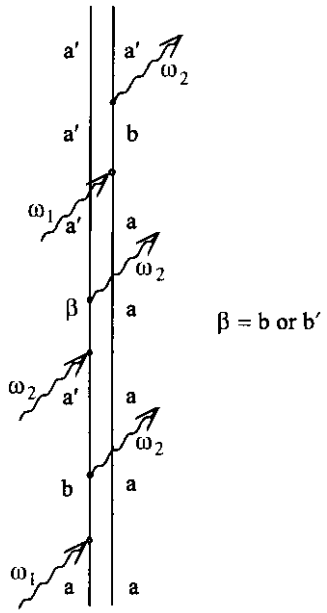

Fig. 8. Sixth-order density matrix diagram for the calculation of the effects associated with the laser power. Case of a resonant interaction: $\beta = b$; case of a non-resonant interaction: $\beta = b'$.

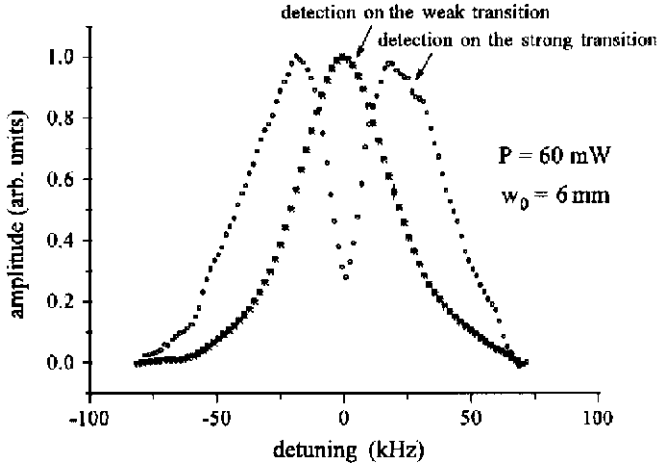

Fig. 9. Lineshapes with high power beams. The power of the beam tuned to the weak transition is $P = 60$ mW and the waist is $W_0 = 6$ mm.

4.3.1 Resonant case: apparent line shape splitting

When the signal is detected on the beam resonant with the strong transition, a dip appears at the center of the line with a depth increasing with the laser power. Figure 9 shows the line shape obtained for the transition $(\varepsilon'' = 5, F'' = 17, J'' = 13) \leftrightarrow (\varepsilon'' = 5, F'' = 16, J'' = 13)$ at the frequency $\Delta/2\pi = 228$ MHz, in two cases where the detection is performed on the strong transition or on the weak transition. In both cases, the power is 60 mW for each beam and the waist radius is 6 mm. This corresponds to a Rabi frequency $\Omega_{ba}/2\pi = 118$ kHz for the strong transition and $\Omega_{ba'}/2\pi = 30$ kHz for the weak transition. In the first case, the line exhibits clearly a central hole whereas in the second case, the line is only broadened. An analogous effect has been reported in [8,9].

Among the 18 main diagrams corresponding to a sixth-order calculation, nine of them correspond to detection on each transition and must be added to the fourth-order Raman line shape. Only five different line shapes are obtained in this calculation (in the case of plane waves):

$$I_1(\Delta) = -\mathrm{Re}\left[\left(\frac{1}{i\Delta + \gamma_{a'a}}\right)^2 \left(\frac{1}{i\Delta + 2\gamma_{ba}}\right)^2\right],$$

$$I_2(\Delta) = -\frac{1}{\gamma_{a'}}\mathrm{Re}\left[\left(\frac{1}{i\Delta + \gamma_{a'a}}\right)\left(\frac{1}{i\Delta + 2\gamma_{ba}}\right)^2\right],$$

$$I_3(\Delta) = -\frac{1}{2\gamma_{ba}\gamma_{a'a}}\mathrm{Re}\left[\left(\frac{1}{i\Delta + \gamma_{a'a}}\right)\left(\frac{1}{i\Delta + 2\gamma_{ba}}\right)\right],$$

$$I_4(\Delta) = -\frac{1}{2\gamma_{ba}\gamma_{a'a}}\mathrm{Re}\left[\left(\frac{1}{-i\Delta + \gamma_{a'a}}\right)\left(\frac{1}{-i\Delta + 2\gamma_{ba}}\right)\right],$$

$$I_5(\Delta) = -\frac{1}{(2\gamma_{ba})^2\gamma_{a'a}}\mathrm{Re}\left[\frac{1}{i\Delta + \gamma_{a'a}}\right].$$

The first term $I_1(\Delta)$ is the only one that leads to a dip in the Raman contribution, because its width is smaller. The other terms contribute to a broadening of the signal.

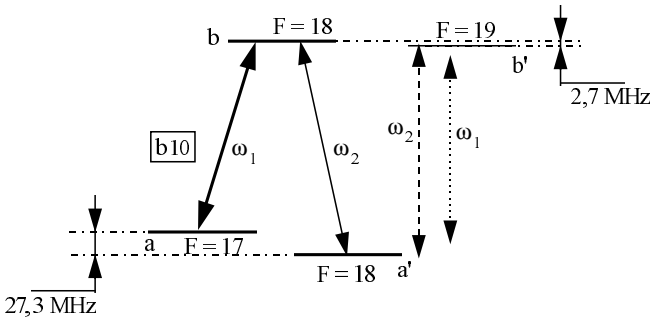

Fig. 10. Representation of the levels involved in the transition $(J''=15, \varepsilon''=3, F''=17) \leftrightarrow (J''=15, \varepsilon''=3, F''=18)$.

Each of the five previous contributions is multiplied by a factor depending on the Rabi frequencies Ω_{ba} and $\Omega_{ba'}$. This amplitude factor is different depending on whether the detected beam is resonant with the strong or with the weak transition. Adding all sixth-order contributions, one finds in each of these two cases:

$$I^{(6)}_{\text{strong}}(\Delta) = \left(2\Omega^2_{ba}+\Omega^2_{ba'}\right) I_1(\Delta) + \left(\Omega^2_{ba'}+\Omega^2_{ba}\right) I_2(\Delta) + \Omega^2_{ba'} I_3(\Delta) + \Omega^2_{ba} I_4(\Delta) + 2\Omega^2_{ba} I_5(\Delta)\ ,$$

$$I^{(6)}_{\text{weak}}(\Delta) = \left(2\Omega^2_{ba'}+\Omega^2_{ba}\right) I_1(\Delta) + \left(\Omega^2_{ba'}+\Omega^2_{ba}\right) I_2(\Delta) + \Omega^2_{ba} I_3(\Delta) + \Omega^2_{ba'} I_4(\Delta) + 2\Omega^2_{ba'} I_5(\Delta)\ .$$

The factor multiplying $I_1(\Delta)$ is greater for a detection performed on the strong transition. Thus, the dip appears preferentially in the first case and not in the second case. To get a quantitative agreement with the experimental data, it is necessary to use a theory in which one of the fields is treated as a strong field, to all orders [10,8].

We may conclude that for a detection on the weak transition, we can use a beam power of a few 10 mW, whereas for a detection on the strong transition, it must not exceed a few mW. For the measurements, we have been generally in the first case.

4.3.2 Light shifts

Each level (a or a') involved in the Raman resonances may be shifted by any optical field which is non-resonant with a transition coupling this level with another one. The magnitude of this shift depends on the Rabi frequency of the non-resonant transition and on the corresponding detuning. In fact, in our measurements, only the two Raman transitions $(J''=13, \varepsilon''=3, F''=16) \leftrightarrow (J''=13, \varepsilon''=3, F''=15)$ and $(J''=15, \varepsilon''=3, F''=17) \leftrightarrow (J''=15, \varepsilon''=3, F''=18)$ may be seriously affected by a non-resonant coupling at ω_2 between the level a' and a perturbing level b' close enough to b ($a' \leftrightarrow b'$ is a strong transition ($\Delta F = \Delta J$)) (Figure 10).

Among the four possible sixth-order diagrams, only the diagram corresponding to Figure 8 with $\beta = b'$ leads to a noticeable result. The quantitative value of the light shift is computed from a resummation of the diagrams [4]. The line shape takes the form

$$I(\Delta) = \mathrm{Re}\left\{ \frac{1}{\gamma_{a'a} + \dfrac{2\gamma_{ba}\Omega^2_{b'a'}}{\omega^2_{b'b}} + i\left(\Delta + \dfrac{\Omega^2_{b'a'}}{\omega_2 - \omega_{b'a'}}\right)} \frac{1}{2\gamma_{ba} + i\Delta} \right\}$$

and the shift of the level a' is given by

$$\delta_{a'} = \frac{\Omega^2_{b'a'}}{\omega_2 - \omega_{b'a'}}\ .$$

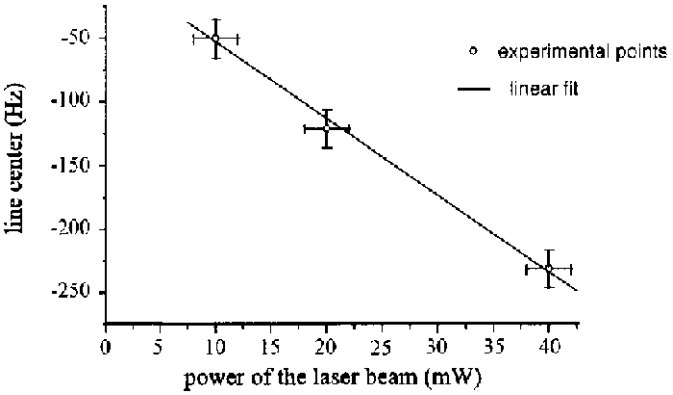

Fig. 11. Light shift of the Raman resonance between the levels $F''=17, J''=15, \varepsilon''=5$ and $F''=18, J''=15, \varepsilon''=5$.

In the case of the transition $(J''=15, \varepsilon''=3, F''=17) \leftrightarrow (J''=15, \varepsilon''=3, F''=18)$, the perturbing level $b'(J'=16, \varepsilon'=3, F'=19)$ is separated from the level b by 2.7 MHz. The calculation of the Rabi frequency, at the center of the beam, is given in [1]. For 20 mW on each beam and a 12.5 mm waist, we find $\Omega_{b'a'}/2\pi \simeq 33$ kHz and $\delta_{a'}/2\pi \simeq -320$ Hz. By taking into account the Gaussian profile of the beams, this result has to be multiplied by about 2/3 to obtain the actual shift: $\delta_{a'}/2\pi = -213$ Hz.

For each measurement, we have used three different powers of the beam resonant with the strong transition in order to control the influence of the power on the resonance frequency. Figure 11 is obtained in the case of the transition $(J''=15, \varepsilon''=3, F''=17) \leftrightarrow (J''=15, \varepsilon''=3, F''=18)$. The uncertainty due to the extrapolation of the line center frequency to zero power is estimated to be 20 Hz.

4.4 Effects associated with molecular frequency changes

Collisions and Zeeman splittings are the main effects of this type.

4.4.1 Influence of molecular collisions

The pressure dependence of the linewidth has been studied previously [1]: a broadening of 7 ± 1 kHz/mTorr

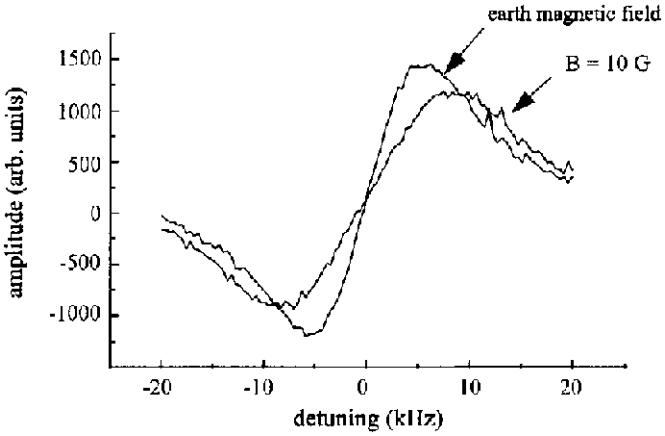

Fig. 12. Line shapes obtained with a 10 G magnetic field and in the earth magnetic field. No shift of the line center is detectable.

(53 ± 8 kHz/Pa) has been found for pressures ranging between 0.3 mTorr (0.04 Pa) and 60 mTorr (8 Pa). Increasing the iodine pressure from 1 mTorr up to 4 mTorr, no pressure shift could be measured with a standard deviation of 15 Hz, whereas the width increased from $\simeq$ 7 kHz to $\simeq$ 28 kHz. Since the working pressure for current measurements was below one milliTorr, we conclude that this source of error may be discarded. It must be emphasized that the line center is not affected by the pumping system: resonance frequency measurements have been performed with or without it, leading to the same results within the accuracy of the experiment.

4.4.2 Influence of the earth magnetic field

It is shown in appendix B that in the case of two linearly orthogonal polarized laser beams, the different Raman resonances associated with Zeeman sublevels are symmetrically located on either side of the resonance center observed in the absence of magnetic field. We have used this polarization configuration to perform our measurements and we have checked experimentally that a magnetic field of the order of 10 Gauss applied horizontally and vertically leads to a broadening of the resonance without any distortion or shift (Fig. 12). So, in the measurement configuration, the earth magnetic field does not produce any detectable shift of the Raman resonance and the associated broadening is close to 200 Hz.

4.5 Summary of the uncertainties

We list in Table 1 the contributions of the various error sources to the global uncertainty for one measurement result. We have classified them, as usual, by their mode of determination: type A, evaluation by statistical methods and type B for all others. The uncertainties are expressed as standard deviations.

Table 1. Uncertainty for the measurements of hyperfine splittings in ground state of I_2.

Type A evaluation
Repeatability: 6 to 28 Hz[(a)]
Reproducibility: 15 Hz
Type B evaluation
Beam divergence: 15 Hz
Beam aberrations: 20 Hz
Light shift (for 2 lines only - see text): (20 Hz)
Synthesizers calibration: < 1 Hz
Combined standard uncertainty (1σ): 28 to 39 Hz[(b)]

[(a)] except for two weak lines for which the repeatability is 53 Hz and 69 Hz.

[(b)] 60 Hz and 75 Hz for the two weak lines.

The repeatability calculated for a series of ten successive measurements ranges from 6 to 28 Hz (with the exception of two weak lines for which it is 70 Hz) according to the signal-to-noise ratio of the resonance under study. The reproducibility has been evaluated from twelve series of ten measurements of a good contrast resonance, performed over one month.

The uncertainty coming from the beam divergence adjustment and from the wave front flatness are estimated to be, respectively, 15 Hz and 20 Hz.

The frequency of the Raman resonance is determined by the frequency difference of the two synthesizers which drive the acousto-optic modulators in Figure 3. The uncertainty of the measurements depends on the stability and on the accuracy of these synthesizers. Both synthesizers are monitored by a G.P.S. frequency reference which ensures an accuracy of 3×10^{-12} and a 3×10^{-10} frequency stability for our 100 s measurement time. The corresponding uncertainty is much smaller than 1 Hz.

The combined uncertainty of all these error sources is about 30 to 40 Hz.

5 Results

5.1 Frequency measurements

Tables 2(a) and 2(b) show sixteen Raman frequencies for each of the ground electronic states $(X, v'' = 0, J'' = 13)$ and $(X, v'' = 0, J'' = 15)$. These results are the means of two series of ten measurements performed a few days apart.

For $J'' = 13$, some of these frequencies can be compared with those obtained by Yokozeki and Muenter in a molecular beam double-resonance experiment [2]. Both techniques give frequencies in a good agreement but the measurement uncertainties of [2], ranging between 100 and 1600 Hz, are significantly larger.

5.2 Hyperfine constants

From the previous measurements, the hyperfine constants have been calculated by a least-squares method and with

Table 2. Measured hyperfine splittings in the ground electronic state of I_2 for the rovibrational levels $v'' = 0$, $J = 13$ and $J = 15$.

Table 2(a)

$J = 13$ Transition $(\varepsilon, F \to \varepsilon, F+1)$	Measured frequency (kHz)	Standard uncertainty (Hz)
$3,15 \to 3,16$	29 293.040	36
$5,13 \to 5,14$	75 377.963	29
$5,11 \to 5,12$	87 249.494	34
$5,14 \to 5,15$	−100 892.328	28
$3,11 \to 3,12$	−129 123.729	35
$3,10 \to 3,11$	−129 254.712	60
$5,15 \to 5,16$	−162 870.115	29
$3,14 \to 3,15$	212 479.080	30
$5,12 \to 5,13$	218 699.102	30
$5,9 \to 5,10$	228 679.163	28
$5,8 \to 5,9$	264 267.940	28
$3,12 \to 3,13$	332 024.930	32
$5,10 \to 5,11$	338 711.688	30
$5,16 \to 5,17$	−348 881.346	28
$3,13 \to 3,14$	−387 971.405	34
$5,17 \to 5,18$	−458 150.320	32

Table 2(b)

$J = 15$ Transition $(\varepsilon, F \to \varepsilon, F-1)$	Measured frequency (kHz)	Standard uncertainty (Hz)
$3,18 \to 3,17$	− 27 275.509	39
$5,16 \to 5,15$	− 64 156.991	28
$5,14 \to 5,13$	− 81 378.475	29
$5,17 \to 5,16$	111 074.922	28
$3,14 \to 3,13$	139 862.066	30
$3,13 \to 3,12$	127 410.928	75
$5,18 \to 5,17$	168 842.674	30
$3,17 \to 3,16$	−209 346.475	29
$5,15 \to 5,14$	−212 921.781	30
$5,12 \to 5,11$	−229 435.863	30
$5,11 \to 5,10$	−278 476.484	30
$3,15 \to 3,14$	−337 556.672	36
$5,13 \to 5,12$	−334 886.301	31
$5,19 \to 5,18$	350 577.535	29
$3,16 \to 3,15$	386 522.359	36
$5,20 \to 5,19$	447 195.796	39

a program described in [3]. No ponderation has been used for the different frequencies. The results are presented in Tables 3(a) and 3(b). For $J = 13$, this new determination of the ground state hyperfine constants is significantly more accurate than previous determinations. However, it is the first time that such an accurate investigation of the hyperfine structure is performed in iodine for two different rotational levels. The comparison between $J'' = 13$ and $J'' = 15$ exhibits a J-dependence of the electric quadrupole constant which may be attributed to a centrifugal distortion of the molecule. The three other constants are remarkably consistent for both J values.

Table 3. Hyperfine constants calculated for $J'' = 13$ (a) and $J'' = 15$ (b).

Table 3(a)

$X, v'' = 0, J'' = 13$	Constants	Uncertainties
eqQ(MHz)	−2452.58514	4.5×10^{-4}
C(kHz)	3.1536	3.3×10^{-3}
d(kHz)	1.528	1.8×10^{-2}
δ(kHz)	3.708	2.2×10^{-2}

Table 3(b)

$X, v'' = 0, J'' = 15$	Constants	Uncertainties
eqQ(MHz)	−2452.59699	4.5×10^{-4}
C(kHz)	3.1543	2.9×10^{-3}
d(kHz)	1.519	1.8×10^{-2}
δ(kHz)	3.701	2.3×10^{-2}

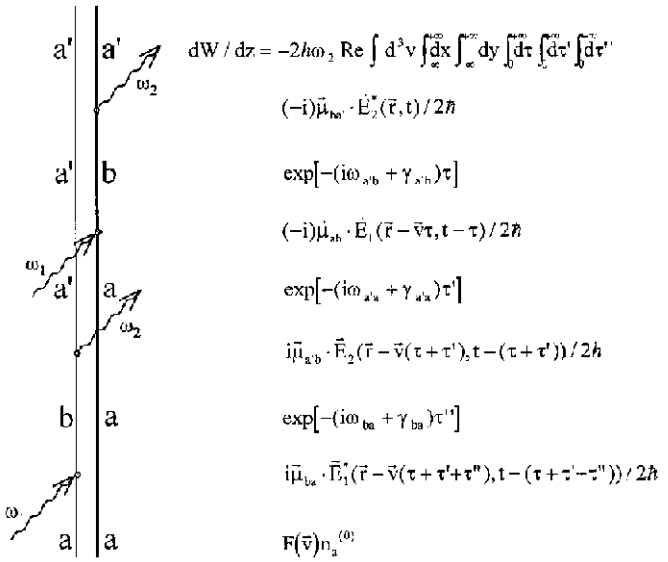

Fig. 13. Fourth-order density matrix diagram for the Raman process

The experimental work described here has been supported in part by the *Conseil Régional d'Ile de France* (LUMINA contract #E-946-95/98).

Appendix A: General expression of the modulated line shape in stimulated Raman spectroscopy

The line shape is derived using the diagrammatic representation of the density matrix evolution and the associated diagrammatic rules [4]. If γ_a, $\gamma_{a'} \ll \gamma_b$, the saturation signal may be neglected and we may take only into account the diagram corresponding to the stimulated Raman process given in figure 13 (see Ref. [1]). The two Gaussian beams (TEM_{00} mode) with optical angular frequencies ω_1 and ω_2 and colinear wave vectors $\overrightarrow{k_1}$ and $\overrightarrow{k_2}$ propagate along the z-axis. The beam j ($j = 1$ or 2) is frequency modulated at the angular frequency ω_{mj} and with a modulation index β_j. The complex representation

of the electric fields is given by

$$\overrightarrow{E_j}(\overrightarrow{r},t) = \overrightarrow{E_j}U_j(\overrightarrow{r})e^{-ik_jz}e^{i\theta_j}e^{i[\omega_j t+\beta_j \sin(\omega_{mj}t)]} = \overrightarrow{E_j}U_j(\overrightarrow{r})e^{-ik_jz}e^{i\theta_j}\sum_n J_n(\beta_j)e^{i(\omega_j+n\omega_{mj})t}. \quad (5)$$

In these expressions:

$$U_j(\overrightarrow{r}) = L_j(z)\exp\left\{-L_j(z)\frac{x^2+y^2}{w_j^2}\right\} \text{ with}$$

$$L_j(z) = \frac{w_j^2}{w_j^2(z)} + i\frac{b_j}{2R_j(z)};$$

w_j and $b_j = k_j w_j^2$ are, respectively, the beam waist radius and the confocal parameter of the beam j;

$w_j(z)$ and $R_j(z)$ are, respectively, the beam radius and the wave front radius of curvature at the position z;

J_n is the n-th-order Bessel function.

Using the notations of reference [1], the power absorbed per unit length for the laser beam 2 is computed from the diagram of Figure 13. Introducing expression (5) for the electric fields, and the intensity factor

$$\Pi_\Omega = \frac{\overrightarrow{\mu_{ba'}}\cdot\overrightarrow{E_2}}{2\hbar}\times\frac{\overrightarrow{\mu_{ab}}\cdot\overrightarrow{E_1}}{2\hbar}\times\frac{\overrightarrow{\mu_{a'b}}\cdot\overrightarrow{E_2}}{2\hbar}\times\frac{\overrightarrow{\mu_{ba}}\cdot\overrightarrow{E_1}}{2\hbar},$$

this absorbed power becomes

see equation (6) next page

The integrations on x, y and $\overrightarrow{v}$ are performed as in reference [1] and yield:

$$\mathrm{d}W/\mathrm{d}z = -n_a^{(0)}\Pi_\Omega\hbar\omega_2(2\sqrt{\pi}/k_1u)S(z)I^{(\mathrm{mod})}(\Delta) \quad (7)$$

with

$$S(z) = \pi L_1(z)L_1^*(z)L_2(z)L_2^*(z)\left(\frac{1}{w_1^2(z)}+\frac{1}{w_2^2(z)}\right)^{-1}$$

and where the general expression for the modulated line shape is given by $I^{(\mathrm{mod})}(\Delta)$:

see equation (8) next page

with $\Delta = \frac{\omega_{ba}}{\omega_1}(\omega_1-\omega_2)-\omega_{a'a}$. The quantity u is the most probable velocity of the Maxwell-Boltzmann distribution in the cell ($u \approx 140$ ms^{-1}at 300 K for iodine). The coefficients A, B and C which depend upon the beam geometry are given by

$$A = \frac{(l_1+l_2^*)(l_1^*+l_2)}{l_1+l_1^*+l_2+l_2^*}, \quad (9)$$

$$B = \frac{l_1^*(l_1+l_2^*)+l_2^*(l_1^*+l_2)}{l_1+l_1^*+l_2+l_2^*}, \quad (10)$$

$$C = \frac{(l_1+l_2)(l_1^*+l_2^*)+4l_1^*l_2^*}{l_1+l_1^*+l_2+l_2^*}, \quad (11)$$

where $l_j(z) = L_j(z)/w_j^2$.

In our case, we have $k_1 \approx k_2$ and expression (8) may be simplified to

see equation (12) next page

which may be written as a single integral:

see equation (13) next page

where:

$$X = [\gamma_{a'a} - i(\Delta + q_1\omega_{m1} - q_2\omega_{m2})]\frac{B}{A}\tau,$$

$$Y = [\gamma_{a'a} - i(\Delta + q_1\omega_{m1} - q_2\omega_{m2})] \times\frac{1}{u\sqrt{A}}\sqrt{1+\left(C-\frac{B^2}{A}\right)u^2\tau^2}$$

and where E_1 is the exponential integral function.

The unmodulated line shape derived in [1] is obtained by letting $\omega_{mj} = 0$ and $\beta_j = 0$ in (12) or (13).

For matched beams ($w_1(z) = w_2(z) = w(z)$; $R_1(z) = R_2(z) = R(z)$), the line shape (12) becomes

see equation (14) next page

It may also be witten as the single integral (13), where:

$$X = [\gamma_{a'a} - i(\Delta + q_1\omega_{m1} - q_2\omega_{m2})]\left(1-i\frac{kw^2(z)}{2R(z)}\right)\tau,$$

$$Y = [\gamma_{a'a} - i(\Delta + q_1\omega_{m1} - q_2\omega_{m2})] \times\frac{w(z)}{u}\sqrt{1+\frac{1}{w^2(z)}\left(1+\frac{k^2w^4(z)}{4R^2(z)}\right)u^2\tau^2}.$$

If the transit time $\tau_{tr} = w(z)/u \gg 1/\gamma_{ba}$, the modulated line shape (14) may be simplified to:

see equation (15) next page

with:

$$T(\Delta) = i\frac{\tau_{tr}}{2}\left\{e^{(i\gamma_{a'a}+\Delta)\tau_{tr}}E_1[(i\gamma_{a'a}+\Delta)\tau_{tr}] - e^{-(i\gamma_{a'a}+\Delta)\tau_{tr}}E_1[-(i\gamma_{a'a}+\Delta)\tau_{tr}]\right\}. \quad (16)$$

However, this simplified line shape does not describe the influence of the beam wave front curvature.

Appendix B: Influence of a magnetic field on Raman resonances in I_2

When the magnetic field is sufficiently weak to neglect the second-order Zeeman effect, the energy shift of the different magnetic sublevels is given by [11]

$$\Delta E(\varepsilon, J, F, M_F) = -g_{\varepsilon,F}\ \mu_n\ B\ M_F, \quad (17)$$

$$\mathrm{d}W/\mathrm{d}z = -2n_a^{(0)}\Pi_\Omega\hbar\omega_2\sum_{p_1}\sum_{q_1}\sum_{p_2}\sum_{q_2}J_{p_1}(\beta_1)J_{q_1}(\beta_1)J_{p_2}(\beta_2)J_{q_2}(\beta_2)\int \mathrm{d}^3vF(\vec{v})\int_{-\infty}^{+\infty}\mathrm{d}x\int_{-\infty}^{+\infty}\mathrm{d}y\mathrm{Re}\int_0^{+\infty}\mathrm{d}\tau$$
$$\times\int_0^{+\infty}\mathrm{d}\tau'\int_0^{+\infty}\mathrm{d}\tau''U_2^*(\vec{r})U_1(\vec{r}-\vec{v}\,\tau)U_2(\vec{r}-\vec{v}\,(\tau+\tau'))U_1^*(\vec{r}-\vec{v}\,(\tau+\tau'+\tau''))$$
$$\times e^{ik_2v_z(\tau+\tau')-ik_1v_z(\tau'+\tau'')}\times e^{-(i\omega_{a'b}+\gamma_{a'b})\tau-(i\omega_{a'a}+\gamma_{a'a})\tau'-(i\omega_{ba}+\gamma_{ba})\tau''}$$
$$\times e^{i[-\omega_2+(q_1-p_1)\omega_{m1}-q_2\omega_{m2}]\tau+i[\omega_1-\omega_2+q_1\omega_{m1}-q_2\omega_{m2}]\tau'+i[\omega_1+q_1\omega_{m1}]\tau''}\times e^{i[(p_1-q_1)\omega_{m1}-(p_2-q_2)\omega_{m2}]t}\,. \tag{6}$$

$$I^{(\mathrm{mod})}(\Delta) = \sum_{p_1}\sum_{q_1}\sum_{p_2}\sum_{q_2}J_{p_1}(\beta_1)J_{q_1}(\beta_1)J_{p_2}(\beta_2)J_{q_2}(\beta_2)\times\mathrm{Re}e^{i[(p_1-q_1)\omega_{m1}-(p_2-q_2)\omega_{m2}]t}$$
$$\times\int_0^{+\infty}\mathrm{d}\tau\int_0^{+\infty}\mathrm{d}\tau' e^{\{i(\Delta+[(k_2/k_1+1)q_1-p_1]\omega_{m1}-q_2\omega_{m2})-(\gamma_{a'b}+\gamma_{ba}k_2/k_1)\}\tau}$$
$$\times\frac{e^{\{i(\Delta+q_1k_2/k_1\omega_{m1}-q_2\omega_{m2})-(\gamma_{a'a}+(k_2/k_1-1)\gamma_{ba})\}\tau'}}{1+Au^2\tau'^2+2Bu^2\tau\tau'+Cu^2\tau^2} \tag{8}$$

$$I^{(\mathrm{mod})}(\Delta) = \sum_{p_1}\sum_{q_1}\sum_{p_2}\sum_{q_2}J_{p_1}(\beta_1)J_{q_1}(\beta_1)J_{p_2}(\beta_2)J_{q_2}(\beta_2)\mathrm{Re}e^{i[(p_1-q_1)\omega_{m1}-(p_2-q_2)\omega_{m2}]t}$$
$$\times\int_0^{+\infty}\mathrm{d}\tau\int_0^{+\infty}\mathrm{d}\tau'\frac{e^{\{i(\Delta+(2q_1-p_1)\omega_{m1}-q_2\omega_{m2})-2\gamma_{ba}\}\tau}\times e^{\{i(\Delta+q_1\omega_{m1}-q_2\omega_{m2})-\gamma_{a'a}\}\tau'}}{1+Au^2\tau'^2+2Bu^2\tau\tau'+Cu^2\tau^2}\,, \tag{12}$$

$$I^{(\mathrm{mod})}(\Delta) = \sum_{p_1}\sum_{q_1}\sum_{p_2}\sum_{q_2}J_{p_1}(\beta_1)J_{q_1}(\beta_1)J_{p_2}(\beta_2)J_{q_2}(\beta_2)\mathrm{Re}e^{i[(p_1-q_1)\omega_{m1}-(p_2-q_2)\omega_{m2}]t}$$
$$\times\frac{\gamma_{a'a}-i\left(\Delta+q_1\omega_{m1}-q_2\omega_{m2}\right)}{2Au^2}\int_0^{+\infty}\mathrm{d}\tau\frac{e^{X-iY}E_1\left(X-iY\right)-e^{X+iY}E_1\left(X+iY\right)}{iY}$$
$$\times e^{\{i(\Delta+(2q_1-p_1)\omega_{m1}-q_2\omega_{m2})-2\gamma_{ba}\}\tau}\,, \tag{13}$$

$$I^{(\mathrm{mod})}(\Delta) = \sum_{p_1}\sum_{q_1}\sum_{p_2}\sum_{q_2}J_{p_1}(\beta_1)J_{q_1}(\beta_1)J_{p_2}(\beta_2)J_{q_2}(\beta_2)\mathrm{Re}e^{i[(p_1-q_1)\omega_{m1}-(p_2-q_2)\omega_{m2}]t}$$
$$\times\int_0^{+\infty}\mathrm{d}\tau\int_0^{+\infty}\mathrm{d}\tau'\frac{e^{\{i(\Delta+(2q_1-p_1)\omega_{m1}-q_2\omega_{m2})-2\gamma_{ba}\}\tau}\times e^{\{i(\Delta+q_1\omega_{m1}-q_2\omega_{m2})-\gamma_{a'a}\}\tau'}}{1+\dfrac{u^2}{w^2(z)}(\tau'^2+2\tau\tau'+2\tau^2)-i\dfrac{ku^2}{R(z)}\tau(\tau+\tau')}\,. \tag{14}$$

$$I^{(\mathrm{mod})}(\Delta) = \sum_{p_1}\sum_{q_1}\sum_{p_2}\sum_{q_2}J_{p_1}(\beta_1)J_{q_1}(\beta_1)J_{p_2}(\beta_2)J_{q_2}(\beta_2)\mathrm{Re}e^{i[(p_1-q_1)\omega_{m1}-(p_2-q_2)\omega_{m2}]t}$$
$$\times\frac{1}{2\gamma_{ba}-i\left[\Delta+(2q_1-p_1)\omega_{m1}-q_2\omega_{m2}\right]}T(\Delta+q_1\omega_{m1}-q_2\omega_{m2}) \tag{15}$$

where: M_F is the projection of the total angular momentum on the direction of the magnetic field $\overrightarrow{B}$,

$\mu_n = 5.05082 \cdot 10^{-27}$ J/T is the nuclear magneton,

$g_{\varepsilon,F} = \sum_I |\alpha(\varepsilon, I, J, F)|^2 g_{I,F}$,

$g_{I,F} = (g_I + g_1) K + g_J (1 - K)$,

$g_I = 1,12$ is the nuclear g-factor,

g_J is the rotational g-factor,

g_1 is the factor allowing for electron screening of a nucleus,

$K = [I(I+1) + F(F+1) - J(J+1)]/2F(F+1)$ results from the angular coupling $\overrightarrow{F} = \overrightarrow{I} + \overrightarrow{J}$.

The gyromagnetic constants g_J and g_1 have been measured for some values of J in the B state in reference [11] and in both the X and B states in reference [12]. We will use the values proposed in this last reference for the state $X, v'' = 0, J'' = 13$ and $J'' = 15$:

$$g_1'' = 0.02 \pm 0.13$$
$$g_J'' = -0.03 \pm 0.04\,.$$

As an example for numerical applications we choose the Raman resonance between the levels $a = (F''=13, \varepsilon''=3)$ and $a' = (F'' = 14, \varepsilon'' = 3)$ of the rotational level $J'' = 15$ of the fundamental vibronic level. The corresponding state vectors can be written, after diagonalisation of the hyperfine Hamiltonian, in the $|J, I, F\rangle$ basis as

$$\begin{aligned}|a\rangle &= 0.81 \times |J''=15, I''=3, F''=13\rangle \\ &\quad +0.59 \times |J''=15, I''=5, F''=13\rangle\,, \\ |a'\rangle &= 0.51 \times |J''=15, I''=1, F''=14\rangle \\ &\quad +0.82 \times |J''=15, I''=3, F''=14\rangle \\ &\quad +0.26 \times |J''=15, I''=5, F''=14\rangle\,.\end{aligned}$$

Using formula (17), we find for the splitting between two Zeeman sublevels 121 Hz/G for the hyperfine level $(F'' = 13, J'' = 15)$ and 70 Hz/G for the hyperfine level $(F'' = 14, J'' = 15)$.

Appendix B.1: Case of two perpendicularly polarized beams

As a first example let us choose a vertical magnetic field and the quantization axis along this direction. One of the beam has a π polarization and the other a σ polarization. Because of this σ polarization, that induces $\Delta M = \pm 1$ transitions, the Raman resonance is split in $2F_a + 1$ couples of Raman magnetic components, as illustrated in Figure 14. The two components of each couple have different intensities:

$$A^+ = \begin{pmatrix} F_b & 1 & F_a \\ -M_a & 0 & M_a \end{pmatrix}^2 \begin{pmatrix} F_b & 1 & F_{a'} \\ -M_a & -1 & M_a + 1 \end{pmatrix}^2 \quad \text{for } M_{a'} - M_a = +1\,;$$

$$A^- = \begin{pmatrix} F_b & 1 & F_a \\ -M_a & 0 & M_a \end{pmatrix}^2 \begin{pmatrix} F_b & 1 & F_{a'} \\ -M_a & 1 & M_a - 1 \end{pmatrix}^2 \quad \text{for } M_{a'} - M_a = -1\,.$$

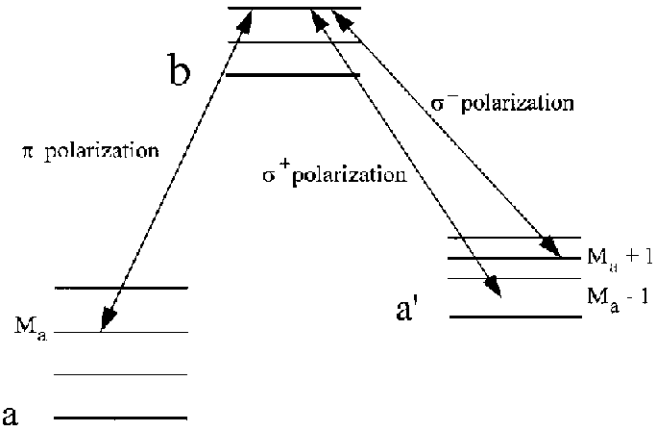

Fig. 14. Levels implied in a magnetic Raman resonance when the two beams are linearly polarized

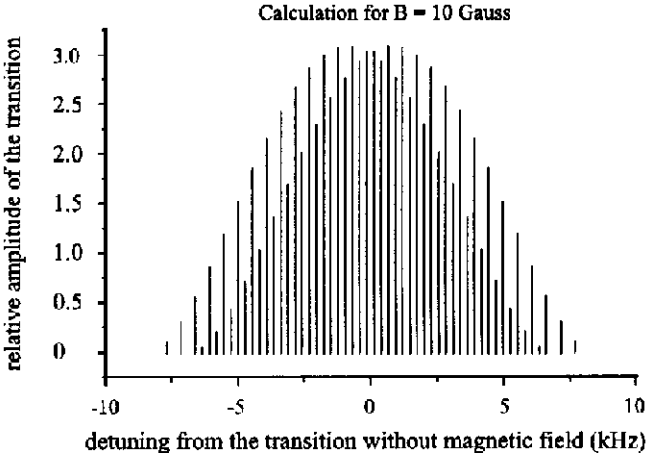

Fig. 15. Amplitude and positions of the magnetic Raman resonances between the levels $F'' = 13$ and $F'' = 14$ for linearly polarized beams and a magnetic field of 10 G.

The frequency splitting between the two components of each doublet is $2\mu_n g_{a'}/h = 140$ Hz/G, for the $F_{a'} = 14$ level. Magnetic doublets are themselves separated by the quantity $\mu_n (g_a - g_{a'})/h = 51$ Hz/G.

These results are summarized by Figure 15, where we have plotted the intensities of the Raman magnetic components as well as their position. We see that the line obtained with this polarization configuration is broadened by the magnetic field, but is not shifted. The same conclusion is reached with other configurations with linear polarizations.

Appendix B.2: Case of two circularly polarized beams

This time, let us choose a magnetic field along the propagation axis. The polarizations of the beams are σ^+ and σ^-. They induce resonances between a level M_a and a level $M_{a'} = M_a + 2$ (Fig. 16)

Each magnetic component has an intensity proportional to the following angular factor:

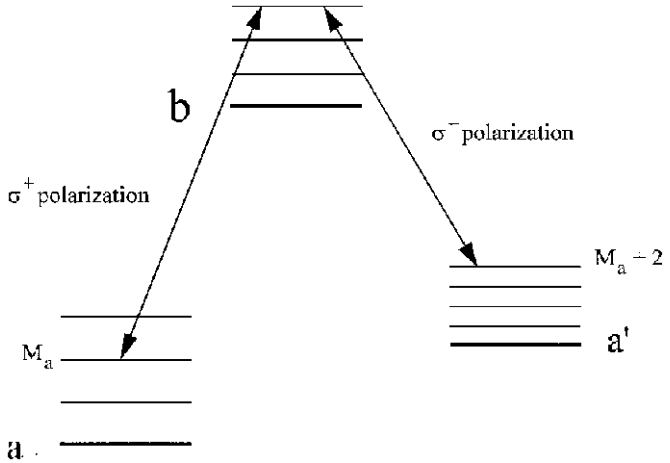

Fig. 16. Levels implied in a magnetic Raman resonance when the two beams are circularly polarized (σ^+ and σ^-).

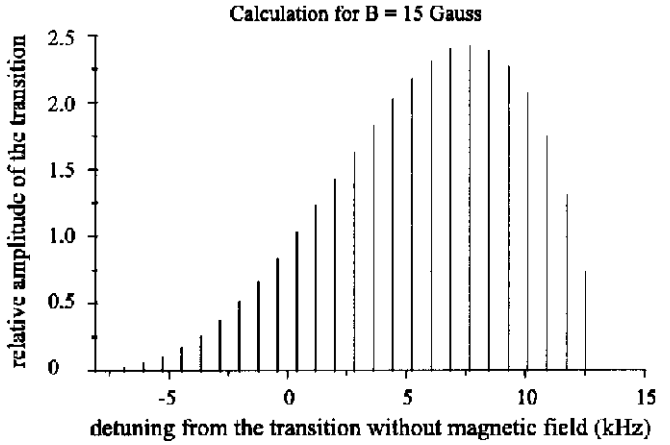

Fig. 17. Amplitudes and positions of the magnetic Raman resonances between the levels $F'' = 13$ and $F'' = 14$ for circularly polarized beams (σ^+ and σ^-) and a magnetic field of 15 G

$$A_M = \begin{pmatrix} F_b & 1 & F_a \\ -M_a - 1 & 1 & M_a \end{pmatrix}^2 \begin{pmatrix} F_b & 1 & F_{a'} \\ -M_a - 1 & -1 & M_a + 2 \end{pmatrix}^2 .$$

A magnetic component is shifted by the quantity

$$\delta = B\mu_n(M_a\,(g_{a'} - g_a) + 2g_{a'})/h\,.$$

The different A_M factors and the position of the resonances are displayed in Figure 17. Unlike the case of linear polarizations, the amplitudes of the different components are not symetrical with respect to the line center. We have plotted in Figure 18 the line shape resulting from the contributions of all the magnetic components, for a magnetic field of 15 G and a Lorentzian line shape 9 kHz wide (HWHM). We clearly see a distortion and the center of the line is shifted by 1.1 kHz. Therefore this is not the good choice of polarization for our measurements.

All these conclusions have been verified experimentally.

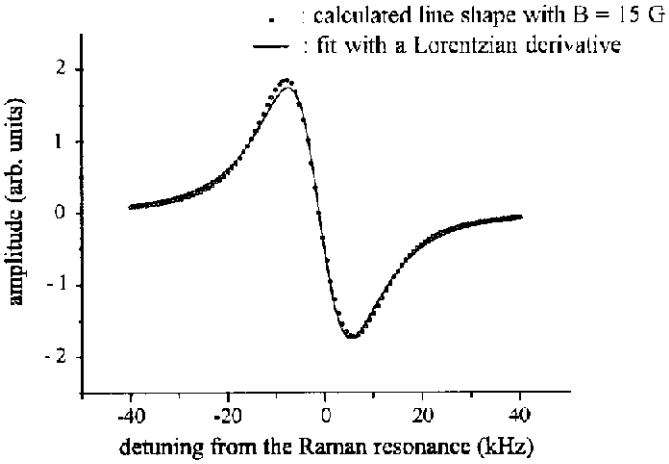

Fig. 18. Calculated line shape, for two circularly polarized beams (σ^+ and σ^-), a 15 G magnetic field and a Lorentzian line shape of 9 kHz (HWHM).

References

1. Ch.J. Bordé, G. Camy, N. Courtier, F. du Burck, A.N. Goncharov, M. Gorlicki, J. Opt. Soc. Am. B **13**, 1837 (1996).
2. A. Yokozeki, J.S. Muenter, J. Chem. Phys. **72**, 3796 (1980).
3. Ch.J. Bordé, G. Camy, B. Decomps, J.-P. Descoubes, J. Vigué, J. Phys. (Paris) **42**, 1393 (1981).
4. Ch.J. Bordé, in *Advances in Laser Spectroscopy*, edited by F.T. Arecchi, F. Strumia, H. Walther (Plenum Publishing Corporation, 1983).
5. F. du Burck, J.-P. Wallerand, B. Mercier, A.N. Goncharov, M. Himbert, Ch. J. Bordé, to be published.
6. M.V. Mantravadi, in *Optical Shop Testing*, edited by D. Malacara, 2nd edn. (John Wiley and sons, 1992).
7. Ch.J. Bordé, G. Camy, B. Decomps, Phys. Rev. A **20**, 254 (1979).
8. R.P. Hackel, S. Ezekiel, in *Laser Spectroscopy IV* (Springer-Verlag, 1978).
9. R.P. Hackel, S. Ezekiel, Phys. Rev. Lett. **42**, 1736 (1979).
10. Ch.J. Bordé, Compt. Rend. Acad. Sci. Paris B **283**, 181 (1976).
11. M. Broyer, J.-C. Lehmann, J. Vigué, J. Phys. (Paris) **36**, 235 (1975).
12. A.N. Goncharov, S.V. Gateva-Kosteva, M.N. Skvorstov, V.P. Chebotaev, Appl. Phys. B **52**, 311 (1991).